Journal of Astronomical Instrumentation, Vol. 5, No. 2 (2016) 1650001 (14 pages)
© The Author(s)
DOI: 10.1142/S225117171650001X

World Scientific
www.worldscientific.com

J. Astron. Instrum. 2016.05. Downloaded from www.worldscientific.com
by CHINESE ACADEMY OF SCIENCES @ BEIJING on 12/13/17. For personal use only.

On-Sky Tests of a High-Power Pulsed Laser for Sodium Laser Guide Star Adaptive Optics

Angel Otarola[*,†,¶¶], Paul Hickson[‡], Ronald Gagné[‡,¶], Yong Bo[§], Junwei Zuo[§], Shiyong Xie[§], Lu Feng[‖], Simon Rochester[**], Dmitry Budker[**,††,‡‡], Shixia Shen[‖], Suijian Xue[‖], Li Min[§§], Kai Wei[§§], Corinne Boyer[*], Brent Ellerbroek[*], JingYao Hu[§], Qinjun Peng[§] and Zuyan Xu[§]

[*]TMT Observatory Corp., Pasadena, 91124, USA

[†]Atmospheric Sciences Department
University of Arizona, Tucson, Arizona, USA

[‡]University of British Columbia, 6224 Agricultural Road
Vancouver, British Columbia V6T 1Z1, Canada

[§]Technical Institute of Physics and Chemistry, Chinese Academy of Sciences
No 2 Beiyitiao Street, Beijing, Zhongguancun, Haidian District, China

[¶]Department of Astronomy and Astrophysics
University of Toronto, 50 Saint George Street
Toronto, ON M5S 3H4, Canada

[‖]National Astronomical Observatories
Chinese Academy of Sciences, 20A Datun Road
Chaoyang District, Beijing, China

[**]Rochester Scientific, LLC, 2041 Tapscott Ave., 94530, USA

[††]Department of Physics, University of California
Berkeley, California 94720, USA

[‡‡]Helmholtz Institute, Johannes Gutenberg University Mainz, Germany

[§§]Institute of Optics and Electronics, Chinese Academy of Sciences, Chengdu, China
[¶¶]aotarola@tmt.org

Received 2015 August 18; Revised 2015 December 2; Accepted 2015 December 10; Published 2016 March 4

We present results of on-sky tests performed in the summer of 2013 to characterize the performance of a prototype high-power pulsed laser for adaptive optics. The laser operates at a pulse repetition rate (PRR) of 600–800 Hz, with a 6% duty cycle. Its coupling efficiency was found to be, in the best test case (using 18 W of transmitted power), 231 ± 14 photons s^{-1} sr^{-1} $atom^{-1}$ W^{-1} m^2 when circular polarization was employed and 167 ± 17 photons s^{-1} sr^{-1} $atom^{-1}$ W^{-1} m^2 with linear polarization. No improvement was seen when D_{2b} repumping was used, but this is likely due to the relatively large laser guide star (LGS) diameter, typically 10 arcsec or more, which resulted in low irradiance levels. Strong relaxation oscillations were present in the laser output, which have the effect of reducing the coupling efficiency. To better understand the results, a physical modeling was performed using the measured pulse profiles and parameters specific to these tests. The model results, for a 10 arcsec angular size LGS spot, agree well with the observations. When extrapolating the physical model for a sub-arcsecond angular size LGS (typical of what is needed for a successful astronomical guide star), the model predicts that this laser would have a coupling efficiency of 130 photons s^{-1} sr^{-1} $atom^{-1}$ W^{-1} m^2, using circular polarization and D_{2b} repumping, for a LGS diameter of 0.6 arcsec Full Width at Half Maximum (FWHM), and free of relaxation oscillations in the 589 nm laser light.

Keywords: Laser guide star, adaptive optics, fluorescence, lasers.

[¶¶]Corresponding author.

This is an Open Access article published by World Scientific Publishing Company. It is distributed under the terms of the Creative Commons Attribution 4.0 (CC-BY) License. Further distribution of this work is permitted, provided the original work is properly cited.

J. Astron. Instrum. 2016.05. Downloaded from www.worldscientific.com
by CHINESE ACADEMY OF SCIENCES @ BEIJING on 12/13/17. For personal use only.

1. Introduction

The use of lasers to create artificial reference stars by means of resonance fluorescence from sodium atoms in the Earth's mesosphere is a well-established technique used in adaptive optics (Roy & Labeyrie, 1985; Jeys, 1991; Fugate *et al.*, 1991; Happer *et al.*, 1994). Either continuous wave or pulsed lasers may be employed. The efficiency of such lasers in exciting sodium depends on many factors, such as the strength and orientation of the geomagnetic field, and the polarization of the laser light (Kibblewhite, 2009; Holzlöhner *et al.*, 2010). High irradiance levels in the sodium region, or narrow spectral linewidth, can lead to sodium saturation, reducing the efficiency. With pulsed lasers, new factors enter including pulse duration, repetition frequency and temporal pulse profile. Efficiency depends on the relation of laser pulse timescales with physical times scales in the sodium region, such as collision rates and Larmor precession.

An important technique that can significantly enhance the sodium return flux, at high irradiance, is D_{2b} repumping. Here a portion, typically in the range 10%–20%, of the laser radiation is shifted in frequency by ~ 1.7 GHz, in order to excite sodium atoms that are in the ground state of the D_{2b} transition to states that decay to the D_{2a} ground state. This can boost the return flux by a factor that can potentially be as high as three Telle *et al.* (2008); Holzlöhner *et al.* (2010). The effectiveness of this technique depends on several factors, including the achieved laser irradiance in the mesosphere.

In this paper, we report on optical tests of a pulsed sodium laser, developed by the Technical Institute of Physics and Chemistry (TIPC) in collaboration with the National Astronomical Observatories of China, both sponsored by the Chinese Academy of Sciences, which is currently being considered for the first-light adaptive-optics system of the Thirty Meter Telescope (TMT) (Ellerbroek *et al.*, 2012, 2013). This solid-state laser, employing sum-frequency Nd:YAG technology, has a repetition rate of up to 800 pulses per second and a duty cycle in the range 6%–10%. The coupling efficiency of this format (the effectiveness with which it excites mesospheric sodium atoms) has been studied theoretically (Rochester *et al.*, 2012). However, uncertainties introduced by the presence of relaxation oscillations, and lack of knowledge of the actual laser guide star (LGS) characteristics, made on-sky testing essential. Laboratory measurements were made to determine the laser characteristics, followed by on-sky observations of the spatial extent, structure and intensity of the LGS. This paper reports results of these tests.

2. Characteristics of the TIPC Pulsed Laser

The laser used for these tests was the TIPC prototype #2. Figure 1 shows the light path and main components and some principal design parameters are listed in Table 1. The laser employs two diode-pumped solid-state Nd:YAG pulsed lasers operating at 1064 nm and 1319 nm wavelength. The beams are combined in a sum-frequency generation (SFG) stage that uses a Lithium Triborate (LiB_3O_3) nonlinear crystal operating in single-pass mode. This provides 589 nm output with average output power of 20 W.

The 1064 nm and the 1319 nm seed lasers employ unidirectional folded ring cavities. These cavities contain two identical diode-pumped laser heads, with each laser head consisting of a Nd:YAG rod illuminated by three diode arrays formed by three Quasi-Continuous Wave (QCW) diode-bars each. Each diode bar delivers 100 W maximum peak power at 808 nm wavelength. The output of the 1064 nm seed laser is expanded and collimated and followed by a power amplifier consisting of two laser pump modules, where each pump module consists of a Nd:YAG rod amplification medium side-pumped by three diode arrays. Each array includes four QCW diode bars having 100 W maximum peak power at 808 nm wavelength. The 1319 nm power amplifier uses two stages, each consisting of two side-pumped QCW laser pump modules of similar characteristics to the one used in the 1064 nm power amplifier. The 1064 nm beam and 1319 nm beams are expanded, collimated, then combined by means of a dichroic mirror. The combined infrared beam is focused inside the LBO crystal to achieve sum frequency mixing. The LBO crystal is a type I non-critical phase matched (NCPM) and has negligible walk-off effect. The LBO crystal in this laser prototype is of dimensions 4 mm × 4 mm × 60 mm and it has a triple band antireflection coating on both faces. The laser components are assembled on an optical breadboard inside a metal enclosure. The laser pump modules are cooled by circulating water that is maintained at 22 ± 0.1°C by a closed-cycle water chiller. A complete technical description of the laser is found in Wang *et al.* (2014).

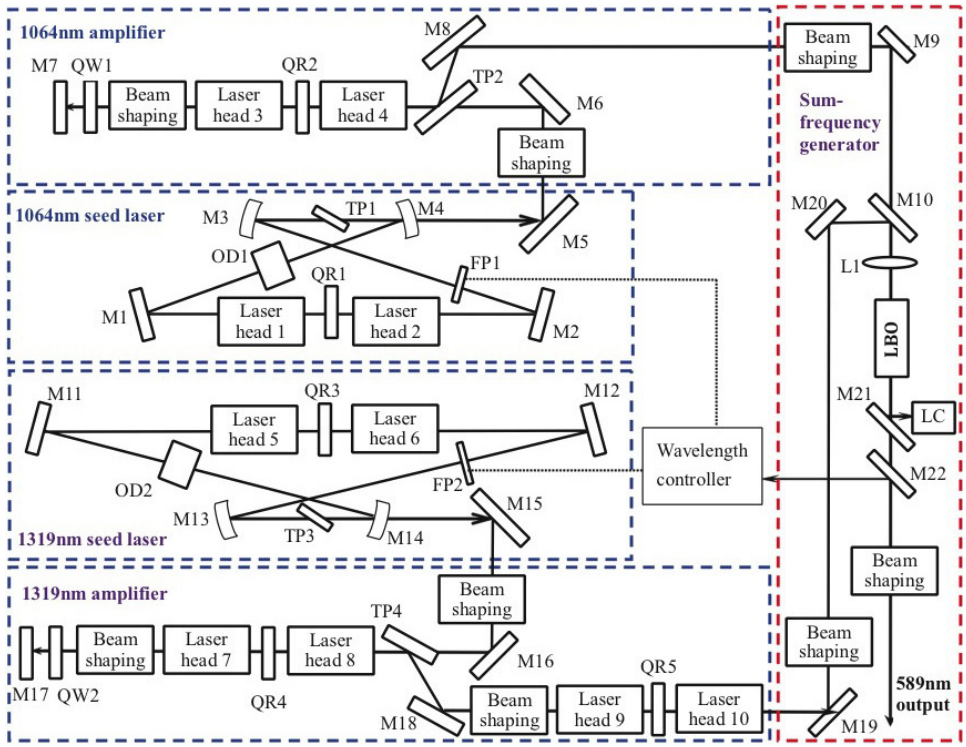


Fig. 1. Block diagram of the TIPC laser prototype #2. The various acronyms in the figure stand for: M = mirror, QW = quarter-wave plate, QR = 90° Quartz Rotator, TP = thin polarizer, FP = Fabry–Perot etalon, LBO = Lithium Triborate (LiB_3O_3) nonlinear crystal, LC = Light Collector point, L = Lens.

Table 1. TIPC laser parameters.

Parameter	Typical value
Average laser power	20 W
Polarization	circular
Pulse length range	75–120 μs
PRR	500–800 Hz
Number of modes	3–5
Mode spacing	254.2 MHz and 215.4 MHz
Beam quality, M_x^2 and M_y^2	1.59, 1.32, at 26 W and 600 Hz
Laser beam diameter	3 mm

The TIPC laser was transported to the Large Zenith Telescope (LZT) facility of the University of British Columbia (Hickson *et al.*, 2007), and installed in a 10,000 clean-room standard laboratory building that was designed and built specifically to support laser testing. This laser room was equipped with all that was necessary to operate the TIPC laser as well as to run specific tests to learn some of its characteristics. The power output of the 1064 nm and 1319 nm lasers, measured shortly after the integration of the laser, were found to be 80 W and 64 W, respectively. The 589 nm output power was measured to be 26 W when operating the laser at a pulse repetition rate (PRR) of 600 Hz and a pulse length of 100 μs, which implies an optical power conversion efficiency in the SFG stage of 18%. When operating the laser at a PRR of 800 Hz, the 589 nm laser output power was measured to be 18 W. The power variability, on a one-minute timescale, was found to be on the order of 4% (one standard deviation).

The pulse temporal profile was measured using a 25 GHz photodiode-detector (Newport 1437M). A beam splitter inserted in the beam transfer optics (BTO) diverted approximately 0.1% of the 589 nm laser light to the photodiode. The photodiode signal was monitored and recorded using a 4 GHz digital oscilloscope (Agilent Infinium DSO 9404A). Measurements were made with the laser operating at a PRR of 600 Hz, and again at 800 Hz. A total of 40 measurements were recorded, each 200 μs long with a resolution of 50 ps, for a total of 4×10^6 data points per measurement. Because of the limited dynamic range of the digital oscilloscope, measurements with two settings of vertical axis resolution were performed: one case with a resolution of 200 mV/division, and another case for a higher resolution and equal to 10 mV/division. The first

J. Astron. Instrum. 2016.05. Downloaded from www.worldscientific.com
by CHINESE ACADEMY OF SCIENCES @ BEIJING on 12/13/17. For personal use only.

J. Astron. Instrum. 2016.05. Downloaded from www.worldscientific.com
by CHINESE ACADEMY OF SCIENCES @ BEIJING on 12/13/17. For personal use only.

setting allowed to capture the whole pulse structure, which was found to be dominated by relaxation oscillations of large amplitude, while the higher intensity resolution was good to capture a more detailed view of the pulse's continuum level.

Typical pulse profiles are shown in Fig. 2. Pronounced relaxation oscillations are seen that last the full duration of the pulse. These generally decrease in amplitude and increase in width during the time evolution of the pulse. A smooth continuum is present, which increases to a maximum value towards the end of the pulse. This continuum is noticeably weaker at 800 Hz PRR than at 600 Hz PRR. The laser pulse lengths were found to be 100 μs and 75 μs, for 600 Hz and 800 Hz, respectively.

Since high-amplitude spikes, caused by relaxation oscillations in the laser cavity, dominate the pulse profiles, the aim was to determine the fraction of the total power contained within these narrow spikes, and the effective duty cycle. For a rectangular pulse train, the duty cycle is defined as the duration of a pulse divided by the period. This corresponds to the fraction of time that the pulse is on, and consequently under that definition the TIPC duty cycle is 6%. It follows that the peak power (the power during the pulse) is greater than the average power by a factor equal to the reciprocal of the duty cycle. However, this result is not applicable to pulses that have a complex shape, such as those shown in Fig. 2, since a good fraction of the energy is contained within spikes that have much shorter duration than the pulse itself.

The energy in the pulse can be obtained by integrating the pulse profile. If this is divided by the peak power (the highest value in the profile, including the effect of the relaxation oscillations), the result gives the effective pulse duration. Dividing this by the pulse period gives an effective duty cycle. When this is done for the pulses shown in Fig. 2, the effective pulse duration is found to be 6.0 μs at 600 Hz and 3.5 μs at 800 Hz. This corresponds to an effective duty cycle of 0.36% at 600 Hz and 0.28% at 800 Hz.

The fraction of power contained in the spikes can be found by integrating the pulse profile and comparing the result with the integral of the profile with the continuum between the spikes. To estimate the continuum signal for the 600 Hz profile, a model of the form

$$V(t) = A\frac{\exp[B(t-t_0)]}{1+\exp[C(t-t_1)]}, \qquad (1)$$

was used. Here $V(t)$ is the continuum signal in V, t is the time in μs, and the parameters A, B, C, t_0 and

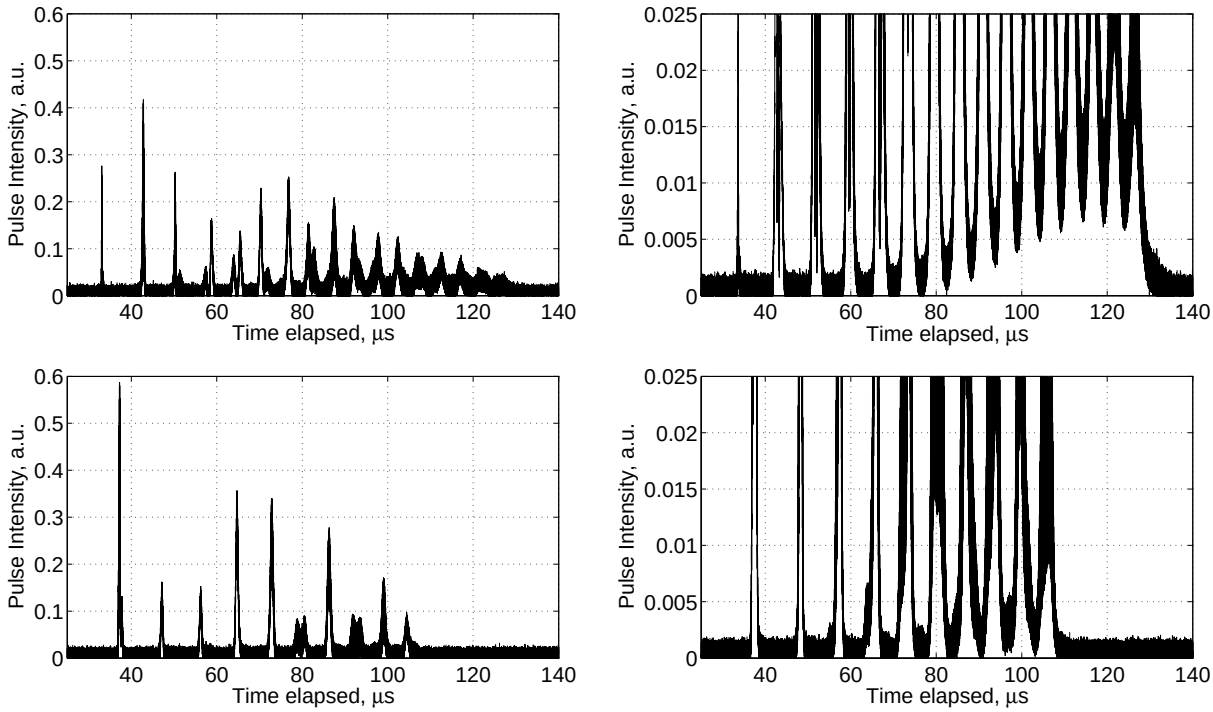


Fig. 2. Pulse structure at PRR 600 Hz (top) and PRR 800 Hz (bottom), for an oscilloscope vertical resolution of 200 mV/division (left), and 10 mV/division (right).

J. Astron. Instrum. 2016.05. Downloaded from www.worldscientific.com
by CHINESE ACADEMY OF SCIENCES @ BEIJING on 12/13/17. For personal use only.

t_1 have the values 0.015, 0.04, 0.3, 100.7 and 121.7, respectively.

Integrating Eq. (1) and comparing it with the integral of the pulse profile, we found that for 600 Hz PRR, the continuum contains approximately 35% of the power. Thus, 65% of the power is contained within the spikes of the relaxation oscillations. For the 800 Hz pulse shown in Fig. 2 (bottom), the continuum is barely visible. For this PPR, the spikes contain almost all of the flux.

Relaxation oscillations are not unusual in long-pulse-length lasers and arise from instability in the development of the power density within the laser cavity. The existence of relaxation oscillations, in 1064 nm and 1319 nm Nd:YAG lasers, has been reported, together with ideas about how to suppress them (Jeys, 1991).

Analysis of the pulse evolution in Fig. 2 (top left) shows that the width of the spikes in the laser power increases from 1 μs to about 5 μs from the beginning to the end of a pulse. The energy in the peaks increases to a maximum about midway through the pulse, and then decreases. Analysis of all the recorded pulses reveals significant variations from pulse to pulse. Both the amplitudes, and the positions of the relaxation-oscillations peaks vary (with respect to the time of the laser trigger). Occasionally, some of the spikes bifurcate, appearing as a double peak.

Interference between different modes excited in the laser cavity can lead to beat frequencies that can be detected in the pulse profile. For a ring cavity, these occur at multiples of $\Delta\nu = c/L$, where c is the speed of light within the cavity and L is the cavity optical path length. Figure 3 shows an expanded view of the first spike that appears in the pulse shown in Fig. 2 (top left). Small oscillations can be seen, and it is also apparent that they are not always present.

Further information can be obtained by analysis of the pulse profiles. The pulse train can be regarded as arising from a modulated stationary stochastic field that can be treated with established statistical methods (von der Linde 1986; Fuss 1994; Schoonover *et al.* 2008). The power spectrum of the pulse intensity is related to the autocorrelation of the laser amplitude spectrum. This contains information on the number and frequency separation of modes and the degree of coherence. The digitized pulses that were recorded for both 600 Hz and 800 Hz PRR were processed this way. For each pulse, the intensity power spectrum was computed

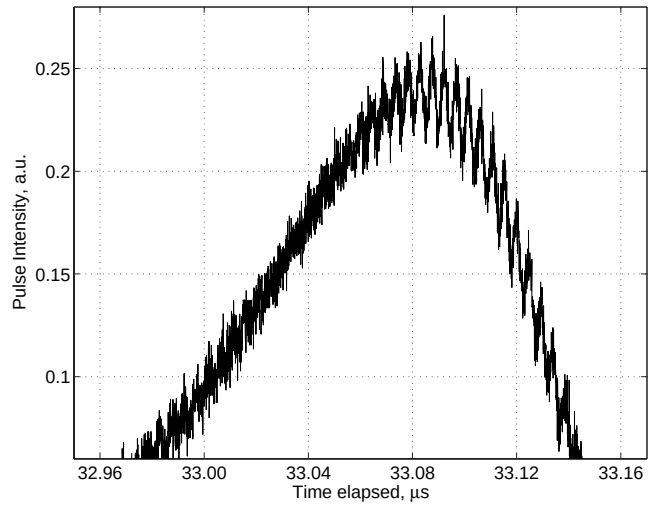


Fig. 3. Expanded view of the left-most spike of the pulse profile shown in the top-left panel of Fig. 2. The high frequency oscillations within the spike have a period of about 4 ns.

and the results averaged for several thousand pulses. An example is shown in Fig. 4. It clearly shows two sequences of narrow peaks, which occur at multiples of 215.4 MHz and 254.2 MHz. The two different mode frequency intervals give values of L equal to 1.392 m and 1.179 m, respectively. These correspond to the optical path lengths of the 1064 nm and 1319 nm cavities. The central peak in the power spectrum contains typically 95% or more of the total energy. The width of the peaks is approximately 1.5 MHz, and the width containing half the total energy is about 4 MHz. These widths represent the line broadening due to the pulse temporal structure, but not the total line width which is determined primarily by the Q of the laser cavity.

The laser line width was measured by means of a scanning confocal Fabry-Pérot interferometer (FPI) (ThorLabs SA200-5B together with a voltage controller ThorLabs SA201). The voltage applied to a piezoelectric actuator in the FPI determines the central wavelength transmission of the interferometer. For this measurement a periodic linear ramp was applied which increases from 0 V to 6 V over 2 s. The corresponding frequency sweep of the voltage ramp was determined to be 400 MHz/V. The transmitted power was detected by a photodiode sensor at the output of the FPI. The amplified photodiode signal, and corresponding ramp voltage, were digitized at a sample rate of 100 kHz by means of a PXI-4472 Data Acquisition Board (DAQ), triggered from the laser controller. For each measurement, 50,000 pulses were recorded over a period of approximately 20 min.

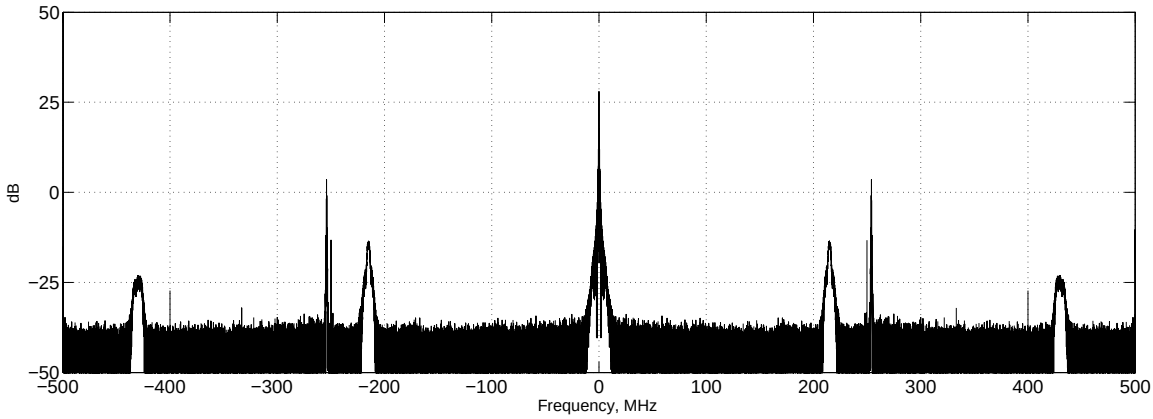


Fig. 4. Power spectrum — an ensemble average of the power spectra obtained of the pulse intensity profiles $P(t)$ of laser pulses is plotted versus frequency ν.

Note: Data gathered when using the laser at 600 Hz PRR.

J. Astron. Instrum. 2016.05. Downloaded from www.worldscientific.com
by CHINESE ACADEMY OF SCIENCES @ BEIJING on 12/13/17. For personal use only.

The line profile was reconstructed by combining measurements from the individual scans. For each pulse, the digitized photodiode signal was integrated to provide the transmitted pulse energy. The corresponding frequency was determined by taking an intensity-weighted average of the ramp voltage during the pulse and converting this to frequency. The resulting profile was averaged in frequency bins of 24 MHz. This was done at both 600 Hz and 800 Hz PRR. In this manner, 50 spectra were obtained for each PRR. Two such spectra are shown in Fig. 5. The figure clearly shows a drift in the laser frequency. Therefore, the 50 spectra were individually aligned in frequency and then averaged. The

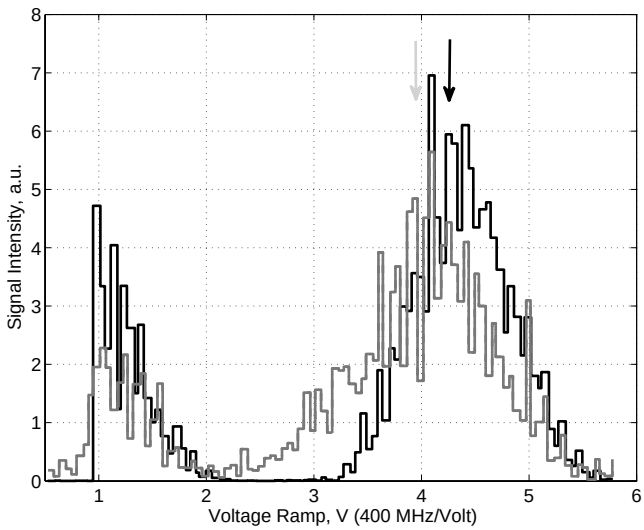


Fig. 5. Two measurements of the TIPC pulsed laser spectra measured with a confocal scanning FPI. The arrows help illustrate the drift in frequency. In this particular example the drift is about 150 MHz.

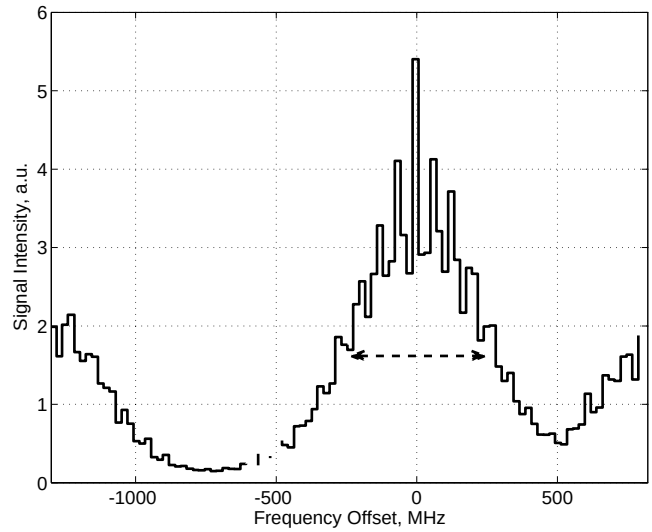


Fig. 6. Average spectral shape of the TIPC pulsed-laser as a function of the scanning voltage ramp of the ThorLabs SA200-5B scanning FPI. The voltage to frequency conversion is 400 MHz/volt. The double-arrow line shows the FWHM spectral width is of order 1.44 V (i.e. 576 MHz).

mean frequency shift was found to be approximately 140 MHz, and the laser line width in the averaged spectrum was in the range 580–600 MHz (Fig. 6). A drift in the laser wavelength, from its optimum value, will have the effect to reduce the laser coupling efficiency to the sodium atoms. Simulations conducted using the physical model described in Rochester *et al.* (2012) show that a 200 MHz reduces the LGS photon flux in about 10%.

3. On-Sky Tests

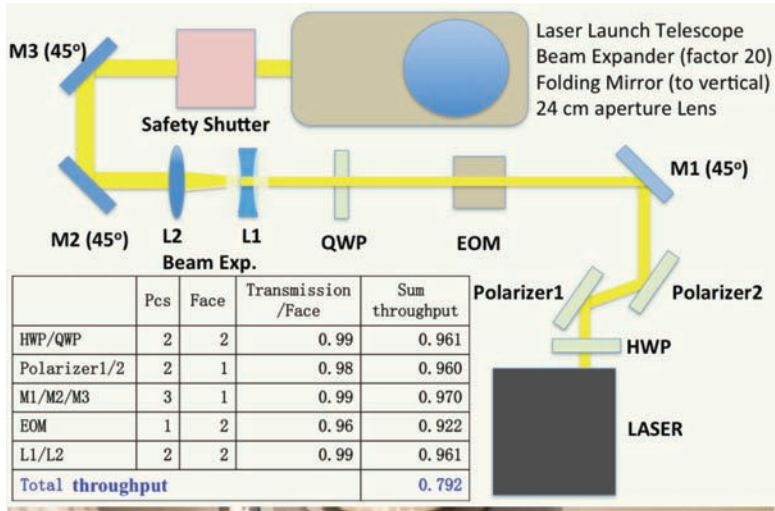
All tests took place at the LZT facility of the University of British Columbia (Hickson *et al.*, 2007).

The LZT is located near the city of Maple Ridge (BC, Canada) at an altitude of 395 m. The observatory coordinates are 122°34.374′ W 49°17.257′ N. It houses a 6 m liquid-mirror telescope equipped with a sodium lidar system that has been used extensively to study the vertical distribution of sodium atoms in the mesosphere (Pfroemmer *et al.* 2009, 2010; Pfroemmer & Hickson 2014). Our plan was to use the LZT Lidar in parallel with the testing of the TIPC pulsed laser, to monitor the sodium column density, a parameter needed for determination of the laser coupling efficiency.

The TIPC laser beam was expanded by a factor of 80 (240 mm in diameter) and projected by means of a combination of BTO and a laser launch telescope (LLT), illustrated in Fig. 7. The BTO includes a quarter-wave (QW) plate, used to induce circular polarization, and an electro-optic modulator (EOM). The EOM allows a portion of the laser radiation to be shifted in frequency in order to implement D_{2b} repumping.

The LLT was designed and built by the Institute of Optics and Electronics, Chinese Academy of Sciences, in Chengdu. The throughput of the BTO plus LLT combination was estimated to be approximately 79%. The LLT employs a two-element diverging lens, mounted on a translation stage for focusing, followed by a 24 cm diameter objective lens. A Zemax ray-trace of the optical system confirmed that it has diffraction-limited image quality when correctly aligned. However, a tolerance analysis showed that the image quality degrades rapidly with even a small degree ($\sim$10 μm) of lateral misalignment of this lens, due to the high optical power and small beam diameter. It was not possible to measure or adjust the alignment in the field as the LLT has no mechanism for this.

The beam at the output of the LLT exited the laboratory vertically through a roof hatch. A polyethylene



	Pcs	Face	Transmission /Face	Sum throughput
HWP/QWP	2	2	0.99	0.961
Polarizer1/2	2	1	0.98	0.960
M1/M2/M3	3	1	0.99	0.970
EOM	1	2	0.96	0.922
L1/L2	2	2	0.99	0.961
Total throughput				0.792

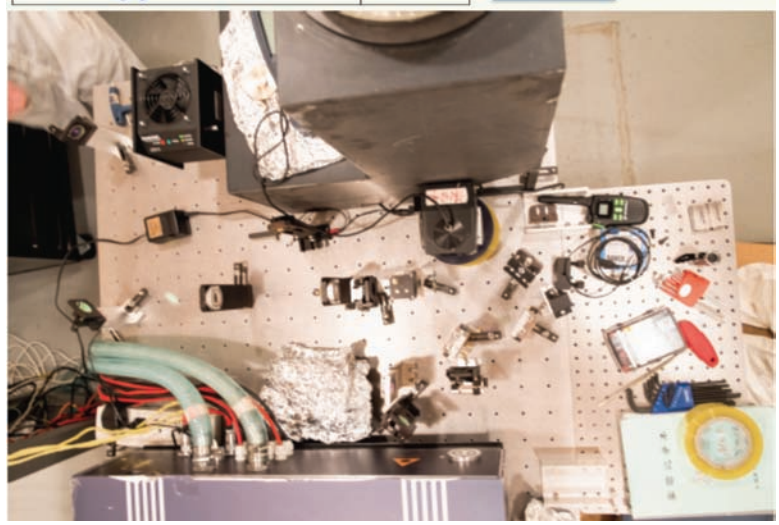


Fig. 7. Block diagram (top) and photograph (bottom) of the BTO and LLT used with the TIPC laser.

J. Astron. Instrum. 2016.05. Downloaded from www.worldscientific.com
by CHINESE ACADEMY OF SCIENCES @ BEIJING on 12/13/17. For personal use only.

J. Astron. Instrum. 2016.05. Downloaded from www.worldscientific.com
by CHINESE ACADEMY OF SCIENCES @ BEIJING on 12/13/17. For personal use only.

barrier was installed surrounding and enclosing the LLT up to the roof, to prevent air escaping through the hatch which might create optical turbulence in the uplink path.

The resulting LGS was observed using the 30 cm auxiliary telescope at the LZT facility. This telescope employs a Ritchey Chrétien optical design with a field flattener. It has a 305 mm clear aperture and 2432 mm focal length. The telescope was equipped with an SBIG ST-7ME CCD camera which has a format of 756×512 pixels. The resulting field of view is 9.6×6.5 arcmin and the pixel size is 0.76×0.76 arcsec. A Baader Planetarium V filter was used in order to facilitate photometric calibration.

During laser propagation, the safety of overflying aircraft was ensured by a combination of aircraft spotters and an X-band radar connected to an interlock system that closes the laser shutter in less than 0.1 s. This combination, approved by Transport Canada, has proven 100% effective in detecting and protecting aircraft that approach the laser propagation path.

Our first observations were used to tune and align the laser and optical components. Then, a series of measurements were made in which the LGS flux was recorded as a function of QW plate rotation angle ϕ. The observed variation was fit with a sinusoid in order to determine the optimal rotation angle.

Science observations were conducted on the nights of the 21st and 22nd of August, 2013. A summary of the laser configurations and observations is given in Table 1. At the start of each night, the laser wavelength was optimized by maximizing the measured LGS intensity. Similarly, the best LLT focus was found by minimizing the full width at half maximum (FWHM) of the LGS image. The results in this manuscript are from observations conducted the night of 21st August 2013, this was the night with the best sky transparency. All measurements were done while propagating the laser along the local zenith direction. For the latitude of the test site, the main geomagnetic field parameters are the following: B-field inclination, 77° 30′ and B-field magnitude 0.525 Gauss.

One purpose of the observations was to investigate the effectiveness of D_{2b} repumping with this laser system. Repumping was achieved by applying a 1713.3 MHz radio-frequency signal to the EOM. The power of this signal was adjusted using an attenuator in order to divert approximately 12% of the laser power to the lower-sideband spectral line, the EOM creates an upper-sideband line of equal power which is not used for the excitation of the sodium. Thus the laser power in the D_{2a} line was reduced by 24% when the EOM was on.

For each power and polarization configuration, one set of images were obtained with the EOM off (no D_{2b} repumping) and a second set with the EOM on, followed by a third set with the EOM off. This approach allowed us to remove any linear drift in either the laser power or the sodium column density.

The 24 tests listed in Table 2 produced a total of 330 images, each having an integration time of 2 s. The total duration of the observations was approximately 75 min and sky conditions appeared to be photometric.

4. Analysis

Each CCD image was preprocessed by subtracting a median dark frame of 2 s integration time, and normalized using a median flat-field frame. The LGS flux was determined by integrating, over a circular aperture, the difference between the intensity and that of the sky background emission. The latter was estimated by computing the median

Table 2. TIPC Laser On-Sky Tests. Observations of August 21st 2013. Last column shows the number of 2 s exposure images taken in the corresponding test.

Test	Time (UTC)	Power (W)	Pol	ϕ (°)	EOM	No
1	08:28:30 – 08:29:54	20	circ	80	off	15
2	08:31:19 – 08:32:43	20	circ	80	on	15
3	08:33:25 – 08:34:49	20	circ	80	off	15
4	08:34:22 – 08:39:49	20	lin	35	off	15
5	08:33:49 – 08:45:08	20	lin	35	on	15
6	08:45:33 – 08:47:05	20	lin	35	off	15
7	08:49:10 – 08:50:48	15	lin	35	off	15
8	08:51:55 – 08:53:31	15	lin	35	on	15
9	08:54:20 – 08:55:58	15	lin	35	off	15
10	08:57:47 – 08:59:24	15	circ	80	off	15
11	09:00:34 – 09:02:03	15	circ	80	on	15
12	09:02:57 – 09:04:30	15	circ	80	off	15
13	09:06:27 – 09:07:56	10	circ	80	off	15
14	09:09:59 – 09:11:28	10	circ	80	on	15
15	09:12:41 – 09:14:14	10	circ	80	off	15
16	09:15:41 – 09:17:07	10	lin	35	off	15
17	09:19:16 – 09:20:45	10	lin	35	on	15
18	09:22:06 – 09:23:39	10	lin	35	off	15
19	10:34:46 – 10:35:34	18	circ	80	off	10
20	10:36:48 – 10:37:42	18	circ	80	on	10
21	10:38:29 – 10:39:22	18	circ	80	off	10
22	10:40:49 – 10:41:43	18	lin	35	off	10
23	10:42:12 – 10:43:06	18	lin	35	on	10
24	10:43:36 – 10:44:29	18	lin	35	off	10

J. Astron. Instrum. 2016.05. Downloaded from www.worldscientific.com
by CHINESE ACADEMY OF SCIENCES @ BEIJING on 12/13/17. For personal use only.

intensity in a nearby region of sky. The radius of the integration aperture was chosen by adjusting the radius until the aperture contained approximately 95% of the total LGS light.

The absolute flux of the LGS was determined by comparing the measured LGS fluxes, in ADC units (ADU), with the corresponding flux from a reference star of known magnitude. Since LGS observations were conducted with the telescope pointing at the zenith, natural stars passing through the field produced trailed images. Examples can be seen in Fig. 8, where the faintest stars have magnitude $V \sim 13$. Two bright stars found in the images for Test 2 and Test 19, respectively, were identified by comparison with the Digitized Sky Survey. The V magnitudes and spectral types of these two stars were obtained from the CDS data center.[a] Data for these stars are given in Table 3.

The spectral photon flux Φ_λ, with units of photons $\mathrm{s^{-1}m^{-2}nm^{-1}}$, for the reference stars was determined as follows. First, the spectral energy distributions $F_{\lambda 0}(\lambda)$ for the corresponding spectral types were found in Pickles (1998), available in digital form from CDS. These spectra are normalized to 1.0 at a wavelength of $\lambda_0 = 555.6\,\mathrm{nm}$. In order to determine the true flux, the product of

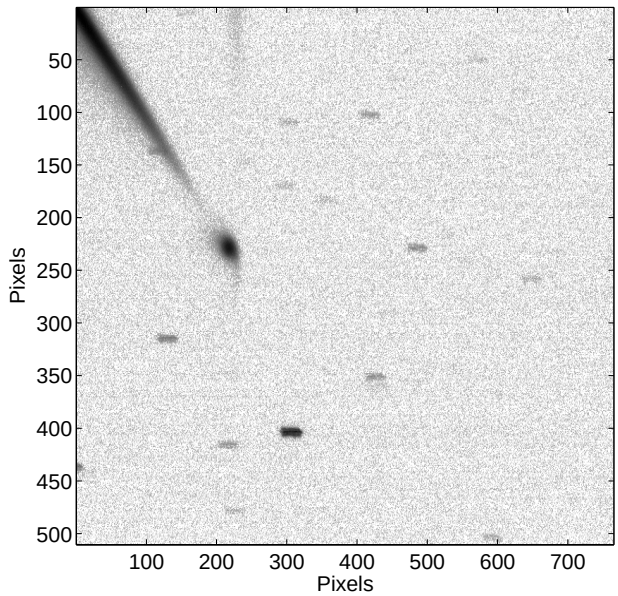


Fig. 8. Example post-processed LGS image. The transmitted laser power was 20 W (9.6 W in the mesosphere), with circular polarization and the D_{2b} repumping. Star trails can also be seen in this 2 s exposure.

[a] http://cdsweb.u-strasbg.fr/.

Table 3. Calibration stars.

Parameter	BD+48 3731	BD+48 135
Right ascension (J2000)	22:26:40.3	00:28:06.0
Declination (J2000)	+49:05:40.3	+49:10:12.0
V magnitude	9.22	9.65
Spectral type	G5III	F5V
Φ_{inst}[ADU]	42967	25774
A [ADU/(photons/s/m^2)]	0.03197	0.02884
$1/AW_{589}$ [ph/s/m^2/ADU]	70.83	78.51

$\lambda F_{0\lambda}/hc$ and the V-band response function $W_V(\lambda)$, from Bessell (1990), was integrated over wavelength to give a normalized photon flux in the V band,

$$\Phi_{0V} = \frac{1}{hc}\int_0^\infty F_{\lambda 0} W_V(\lambda)\lambda \mathrm{d}\lambda. \tag{2}$$

The same was then done for the Spectral Energy Density (SED) of an A0 type star to give $\phi_{0V}^{\mathrm{Vega}}$. The photon flux at 555.6 nm received, at the top of the Earth's atmosphere, from an A0 star having $V = 0$ is $\phi_\lambda^{\mathrm{Vega}}(\lambda_0) = 9.40 \times 10^7$ photons $\mathrm{s^{-1}m^{-2}nm^{-1}}$ (Oke & Schild, 1970). Therefore, the photon flux from the reference star, at 5556 Å, is given by

$$\Phi_\lambda(\lambda_0) = 10^{-0.4\,V}\left(\frac{\Phi_{0V}^{\mathrm{Vega}}}{\Phi_{0V}}\right)\Phi_\lambda^{\mathrm{Vega}}(\lambda_0). \tag{3}$$

The term in parenthesis is the required correction due to the spectral type of the reference star.

The absolute photon flux from the reference star at any wavelength is then found from

$$\Phi_\lambda(\lambda) = \frac{\lambda F_\lambda(\lambda)}{\lambda_0 F_\lambda(\lambda_0)}\Phi_\lambda(\lambda_0). \tag{4}$$

The instrumental flux measured from the CCD image, in ADC units, is given by

$$\Phi_{\mathrm{inst}} = A\int_0^\infty \Phi_\lambda W(\lambda)\mathrm{d}\lambda. \tag{5}$$

Here, A is a proportionality constant related to the telescope area and throughput, CCD gain and atmospheric transmission. The response function $W(\lambda)$ is the product of the filter transmission function and CCD quantum efficiency. (We ignore the wavelength variation of atmospheric and telescope transmission, which is small over our bandwidth).

$W(\lambda)$ can be computed using tabulated values of the Baader V-filter transmission and the CCD quantum efficiency, and Φ_{inst} is determined by integrating the CCD pixel intensity values (in ADC units) over the star trail. Thus, from Eq. (5), we

J. Astron. Instrum. 2016.05. Downloaded from www.worldscientific.com
by CHINESE ACADEMY OF SCIENCES @ BEIJING on 12/13/17. For personal use only.

obtain the proportionality constant A, which is listed in Table 3.

The photon flux Φ (in the mesosphere), in photons s^{-1} m^{-2}, of the LGS can now be determined from the instrumental flux Φ_{inst} according to

$$\Phi = \frac{\Phi_{inst}}{AW_{(589\,nm)}}, \quad (6)$$

where $W_{589\,nm}$ is the value of the response function at 589 nm.

In addition to the LGS flux, the FWHM of the intensity profiles were measured along the horizontal (E–W) and vertical (N–S) directions in the image. Figure 8 shows a post-processed image of the LGS spot generated with the TIPC laser for circular polarization and an output laser power of 20 W (power measured before the BTO).

The efficiency with which the laser excites sodium is described by the coupling efficiency s_{ce}, which is the photon emission rate per steradian from a single atom, per W m^{-2} of laser irradiance in the mesosphere. It is given by Holzlöhner *et al.* (2010).

$$s_{ce} = \frac{\Phi L^2}{PT_a^X C_{Na} X}. \quad (7)$$

Here, P is the transmitted laser power in W, C_{Na} is the column density of atomic sodium, T_a is the atmospheric transmission at zenith, at a wavelength of 589 nm, L is the distance to the sodium layer, and X is the air mass (equal to the secant of the zenith angle). The coupling efficiency has units of photons s^{-1} sr^{-1} $atom^{-1}$ W^{-1} m^2.

T_a, derived from observation of standard stars at various elevation angles, was found to be 0.8 for the night of our observations. For comparison, the atmospheric transmission at 589 nm, at a good quality astronomy site such as Paranal in northern Chile is about 0.9, as possible to derived from atmospheric extinction information in Patat (2004). Scaling the value of the atmospheric transmission by the difference in geographic altitude between the Paranal site (2540 m a.s.l.) and the LZT site (395 m a.s.l.) matches quite well our observations for the atmospheric transmission.

The transmitted power P was obtained by multiplying the measured laser power by the throughput of the BTO/LLT combination. L was taken to be the difference between the mean sodium altitude of 91.6 km Pfroemmer & Hickson (2014) and the LZT altitude of 395 m.

The sodium column density exhibits seasonal and diurnal variations, and is also latitude dependent (e.g. States *et al.*, 1999; Plane *et al.*, 1999; She *et al.*, 2000; Prasanth *et al.*, 2009). Our plan was to use the LZT lidar to measure the sodium column density, and vertical distribution, at the same time as the observations made with the TIPC laser. However, the power amplifier quartz dye cell in the LZT laser system cracked just as we were starting the on-sky tests, precluding this possibility. We therefore adopted a column density of 2.5×10^{13} atoms m^{-2}. This is typical mean value and is consistent with airglow measurements by the ODIN satellite, for the LZT latitude (49°N) and the month (August) of observations (Fan *et al.* 2007; Gumbel *et al.* 2007; Hedin & Gumbel 2011). Further support to the Na column density adopted for this analysis, comes from the composite climatology of Na density in the mesopause of She et al. She *et al.* (2000), that provides a mean value of 2.68×10^{13} atoms m^{-2} for the month of August and at the latitude of Fort Collins (CO, 41°N).

5. Results

The photometric calibration derived from the two stars listed in Table 3, give zero-point coefficients A that agree with each other to within 11%. The difference is likely due to a combination of atmospheric transparency variations, scintillation, catalog and measurement errors. We decided to use the mean of the two values, which results in a standard error of 7%. We believe that this is a fair estimate of the accuracy of our photometry.

The calibrated LGS fluxes Φ are plotted versus laser power in Fig. 9 and irradiance in Fig. 10. The irradiance was estimated by multiplying the average laser power within each pulse by the BTO/LLT throughput and atmospheric transparency, then dividing by the product of the laser beam area in the mesosphere. The latter was determined by subtracting in quadrature the seeing FWHM, measured from star images, from the measured LGS FWHM. The area used is that enclosed within the FWHM.

Despite a significant amount of scatter, a clear enhancement can be seen in the photon flux when using circular polarization. However, the results show no obvious increase when Na D_{2b} repumping is employed (EOM on). In order to assess the statistical significance, we show in Table 4 mean LGS fluxes for circular and linear polarization, for laser power levels ranging from 10 W to 20 W. The flux is typically about 40% greater using circular polarization, a gain

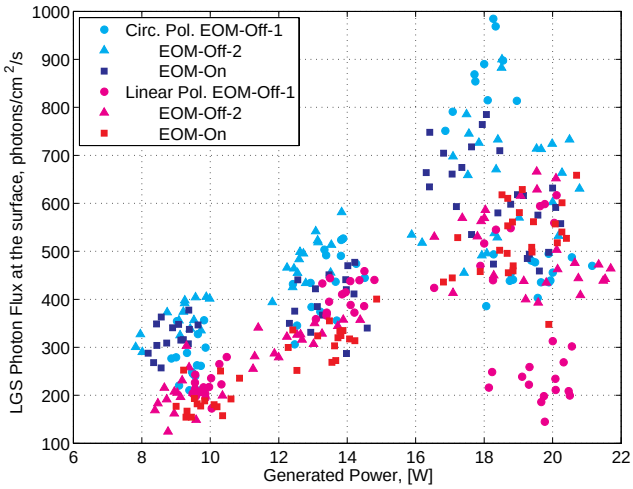


Fig. 9. LGS flux Φ, as a function of generated laser power, at 600 Hz PRR. Blue and cyan symbols indicate circular polarization while red and magenta indicate linear polarization. Square symbols indicate that 12% D_{2b} repumping was employed.

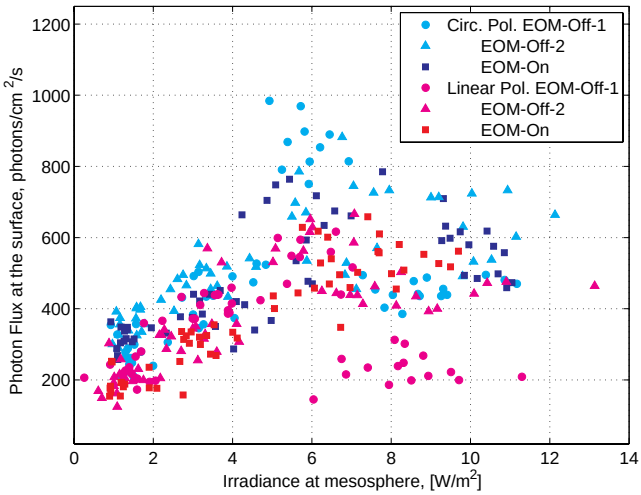


Fig. 10. LGS flux, as for Fig. 9, but plotted versus laser irradiance in the mesosphere.

Table 4. LGS flux (ADU) versus polarization.

Laser power (W)	10	15	18	20
Mean flux, circular	47198	65241	102340	79855
Mean flux, linear	30198	51724	75453	58055
Gain with circ. pol. (%)	+56.3	+26.1	+35.6	+37.6
Std. error in gain (%)	3.9	2.9	3.7	3.5

that is more than ten times the measurement error. This confirms the theoretical expectation that circular polarization is more efficient than linear polarization Holzlöhner *et al.* (2010).

Table 5. LGS flux (ADU) versus EOM state for circular polarization.

Laser power (W)	10	15	18	20
Mean flux, EOM off	46874	68270	106112	78600
Mean flux, EOM on	47845	59185	94784	82366
Std. dev., EOM on	5090	8259	6556	8661
Repumping gain (%)	+2.1	−13.3	−10.7	+4.8
Std. error in gain (%)	2.8	3.1	2.0	2.9

Table 6. LGS flux (ADU) versus EOM state for linear polarization.

Laser power (W)	10	15	18	20
Mean flux, EOM off	31218	54011	75307	50019
Mean flux, EOM on	28158	47151	75744	74129
Std. dev., EOM on	4775	5412	10216	8400
Repumping gain (%)	−9.8	−12.7	+0.6	+48.2
Std. error in gain (%)	4.0	2.6	4.3	4.3

An analysis of the effect of repumping is shown in Tables 5 and 6. It is evident that in all but one case there is no significant enhancement of the LGS flux with the EOM on. In fact in three cases there appears to be a marginally significant reduction in flux with the EOM on, which might be due to the reduced laser power at the D_{2a} wavelength when repumping. The exception is the case of linear polarization and 20 W laser power, where there appears to be a 10-sigma enhancement when the EOM is on. However, it should be noted that even with the EOM on, the flux is less than that seen at the lower power of 18 W, with the EOM on or off. Rather than an enhancement due to the EOM, it appears that this is the result of a reduction in flux for the measurements taken with the EOM off at 20 W and linear polarization. The cause of this reduction is unknown. Additional tests could resolve this, but the weather did not permit further observations.

The coupling efficiency of the TIPC laser, is shown as a function of generated laser power in Fig. 11 and mean values are reported in Table 7. In the table, the observed LGS angular diameters (FWHM) are listed, as well as the physical diameters and irradiance in the mesosphere.

Table 7 shows the LGS FWHM to decrease with increasing laser power, this effect was investigated and it was found to be likely the results of thermal lensing affecting one of the optical elements in the Laser Launch Telescope (LLT). The focus

J. Astron. Instrum. 2016.05. Downloaded from www.worldscientific.com
by CHINESE ACADEMY OF SCIENCES @ BEIJING on 12/13/17. For personal use only.

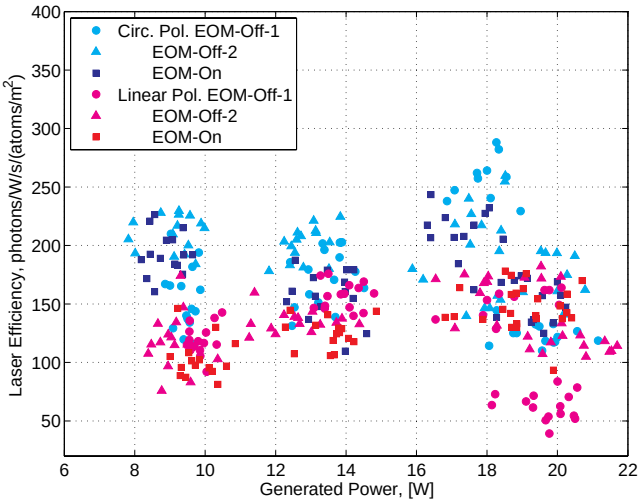


Fig. 11. Coupling efficiency s_{ce} as a function of generated laser power., at 600 Hz PRR. Blue and cyan symbols indicate circular polarization while red and magenta indicate linear polarization. Square symbols indicate that 12% D_{2b} repumping was employed.

Table 7. Laser coupling efficiency (S_{ce}, photons s^{-1} sr^{-1} $atom^{-1}$ W^{-1} m^2).

Laser power (W)	10	15	18	20
LGS FWHM (arcsec)	21.5	16.2	14.0	12.1
LGS FWHM (m)	9.3	6.9	5.9	5.0
Peak irradiance (W m^{-2})	1.5	4.2	7.0	10.9
S_{ce}, Cir. pol. no repumping	222	212	230	177
S_{ce}, Cir. pol. 12% repumping	204	167	231	164
S_{ce}, Lin. pol. no repumping	125	165	160	125
S_{ce}, Lin. pol. 12% repumping	109	132	167	148

stage of the LLT was adjusted with the laser operating at high power. When testing the laser at lower transmitted powers, the laser power density on the optical components in the BTO and LLT is lower. Thermal lensing effects, due to a combination of deformation and change in index of refraction, can cause significant spatial variations in optical path length (Mansell *et al.*, 2001). The first and smallest-diameter lens in the LLT is made from BK-7 glass, which has a relatively-small refractive-index temperature coefficient of $2.4 \times 10^{-6}\,C^{-1}$, but has 15 times the thermal expansion coefficient of fused silica. Differential thermal effects in this lens can produce significant defocus. We found that adding five waves of curvature to the first surface of this lens would produce 9 arcsec of defocus. This is consistent with the thermal variations expected from changes in laser power density (no refocusing of the LLT was done at low power, since the main interest is to test the laser at its highest power level). The LLT has since been redesigned to avoid this problem.

6. Discussion

It is possible that the lack of flux enhancement with D_{2b} repumping is a result of the relatively low laser irradiance, due to the large LGS size. To investigate this, physical modeling was performed. The model of (Rochester *et al.*, 2012) was used with parameters specifically chosen to match the conditions of the laser tests, including using the actual measured pulse profile of the TIPC laser. The adopted parameters are listed in Table 8. It is important to notice that during daytime adjustments of the EOM, and its RF driver tuning, prior to the observations, some drift in power and frequency of the RF driver was observed. Besides, in the on-sky tests reported in this study, the D2b repumping offset was set to 1713.3 MHz as was agreed to be the optimum frequency offset (S. Rochester, *private communication*). Recent on-sky tests (D. Bonaccini Calia, *private communication*) show that the frequency offset for optimum repumping of the Na D2b line seems to be 1717.8 MHz, see Table 1 (Holzlöhner *et al.*, 2010). Because of these we cannot rule out the

Table 8. Parameters used for physical modeling of the TIPC pulsed laser.

Parameter	Value
PRR (Hz)	600 Hz
Pulse length	100 μs
BTO/LLT Throughput	0.6
Atmospheric transmission	0.8
Na centroid altitude (km)	92 km
Na layer thickness (FWHM) (km)	10 km
Na column density	2.5×10^{13} atoms m^{-2}
Observatory m.s.l. altitude	395 m
Geomagnetic field strength	0.525 G
Geomagnetic field declination (+ East)	+16°57′
Geomagnetic field inclination (+ Down)	+70°30′
Angle between laser light propagation direction and magnetic field direction	90° + 70°30′ = 160°30′
Temperature at Na centroid altitude	195 K
N_2 density at Na centroid altitude	4×10^{19} atoms m^{-3}
O_2 density at Na centroid altitude	1×10^{19} atoms m^{-3}
Frequency offset for D2b repumping	1713.3 MHz

J. Astron. Instrum. 2016.05. Downloaded from www.worldscientific.com
by CHINESE ACADEMY OF SCIENCES @ BEIJING on 12/13/17. For personal use only.

J. Astron. Instrum. 2016.05. Downloaded from www.worldscientific.com
by CHINESE ACADEMY OF SCIENCES @ BEIJING on 12/13/17. For personal use only.

possibility that the D2b repumping may not have been performed with optimal efficiency.

The sodium density was assumed to have a Gaussian dependence on altitude. The density and temperature as a function of altitude for N_2 and O_2 were obtained from the MSIS-E-90 atmospheric model using the site coordinates of the LZT.

The response of the sodium atoms to a laser pulse is calculated for a range of intensities and altitudes in the sodium layer. These results are then integrated over the transverse and longitudinal extent of the laser beam for a particular total light power and LGS spot size. This gives the observed flux at the surface. The coupling efficiency s_{ce} is then obtained from Eq. (7). The results are shown in Table 9.

Importantly, the return flux for linearly polarized light depends on the polarization angle. For this study, one specific angle was used: the polarization direction was assumed to be in the plane defined by the light propagation direction and the direction of the magnetic field, i.e. the light polarization pointed in the direction of the component of the magnetic field that was perpendicular to the light propagation direction. A sensitivity study showed that the LGS flux return fluctuation, due to the uncertainty in the angle between the linearly polarization direction and the B-field vector, was smaller than the overall uncertainty in the calculated results.

The coupling efficiencies estimated from the on-sky tests, shown in Table 7, are on average about 30% lower than those predicted by the physical model, shown in Table 9. This could be explained if the actual column density of atomic sodium, during the observations, was lower than the adopted value. A column density of 1.8×10^{13} atoms m^{-2} would give the best agreement with the model. This is well within the natural variability of the atomic sodium abundance. If using this value of the column density, the coupling efficiencies shown in Table 7 increase by a factor of 2.5/1.8 (~ 1.4). The residual differences are then in the range $\pm 25\%$. These differences might be attributed to pulse-to-pulse fluctuations in the laser pulse format, such as variations in the strength of the relaxation oscillations and mode hopping in the laser cavities. The relative variations with laser power, polarization and repumping should be reliable and these also agree well with the model predictions.

The agreement between the observed and modeled coupling efficiency motivated us to extend the modeling to a smaller LGS angular diameter, with and without relaxation oscillations. The model was run assuming circular polarization, with and without D2b repumping. The results are shown in Table 10. The term "Square pulse" indicates an ideal pulse profile that has constant power within the pulse and no relaxation oscillations. "Measured pulse" means the actual TIPC pulse profile, including the relaxation oscillations.

It can be seen from these results that the relaxation oscillations seen in the TIPC laser significantly reduce the coupling efficiency. This is likely a result of sodium layer saturation and stimulated emission, which becomes important at the high power levels present within the relaxation spikes. One can make a rough estimate of the degree of saturation by considering the radiative energy density in the mesosphere during a spike. At 800 Hz PRR, and 20 W average power, each laser pulse contains an energy $W \simeq 25$ mJ. The effective pulse duration of $\tau \simeq 3.5\,\mu$s, found in §2, results in a peak spectral energy density, for a gaussian beam profile, of $U_\nu \simeq 4 \ln 2 W/\pi w^2 c\tau\Delta\nu$, where w is the beam FWHM and $\Delta\nu$ is the laser linewidth. Taking $w = 0.3$ m (0.6 arcsec) and $\Delta\nu = 6000$ MHz, we obtain a peak energy density on the order of $4 \times 10^{-13}\,\mathrm{W m^{-3}\,Hz^{-1}}$. This should be compared with the natural energy density $U_{\nu 0} = 8\pi h/\lambda^3 \simeq 8.15 \times 10^{-14}$ for which the rates of stimulated and

Table 9. Modeled laser coupling efficiency (S_{ce}, photons $\mathrm{s^{-1}\ sr^{-1}\ atom^{-1}\ W^{-1}\ m^2}$).

Laser power (W)	10	15	18	20
Observed LGS FWHM (arcsec)	21.5	16.2	14.0	12.1
LGS FWHM in mesosphere (m)	9.3	6.9	5.9	5.0
Peak irradiance ($\mathrm{W\,m^{-2}}$)	1.5	4.2	7.0	10.9
S_{ce}, Cir. pol. no repumping	280	290	290	290
S_{ce}, Cir. pol. 12% repumping	230	220	270	280
S_{ce}, Lin. pol. no repumping	230	220	210	190
S_{ce}, Lin. pol. 12% repumping	200	200	200	190

Table 10. Predicted laser coupling efficiency for a 0.6 arcsec FWHM LGS with circular polarization, 20 W laser power, 800 Hz PRR and 87 μs pulse length (photons $\mathrm{s^{-1}\ sr^{-1}\ atom^{-1}\ W^{-1}\ m^2}$).

C_{Na} (atoms $\mathrm{m^{-2}}$)	2.5×10^{13}
Measured pulse, no repumping	50
Measured pulse, 12% repumping	90
Square pulse, no repumping	70
Square pulse, 12% repumping	130

spontaneous emission are equal. For a two-level atom, the upper-state occupation probability is given by $1/(U_{\nu 0}/U_{\nu}+2)$, which saturates at a value of 1/2. We see that for a 0.6 arcsec FWHM, the relaxation oscillations will result in significant saturation of the atomic sodium, about 90% of the fully-saturated value. Mitigating or eliminating the relaxation oscillations will be a priority for future development of the TIPC laser.

Acknowledgments

Gordon and Betty Moore Foundation; Canada Foundation for Innovation; Ontario Ministry of Research and Innovation; National Research Council of Canada, the Natural Sciences and Engineering Research Council of Canada; British Columbia Knowledge Development Fund; Association of Universities for Research in Astronomy; U.S. National Science Foundation; National Natural Science Foundation of China under Grant No. 11303056.

We gratefully acknowledge the support of the Thirty Meter Telescope project and its collaborating institutions. These are the Association of Canadian Universities for Research in Astronomy, the California Institute of Technology, the University of California, the National Astronomical Observatory of Japan, the National Astronomical Observatories of China and their consortium partners, and the Department of Science and Technology of India and their supported institutes. Valuable technical assistance was provided by the Technical Institute of Physics and Chemistry of the Chinese Academy of Sciences.

We thank two anonymous reviewers for their careful reading of this manuscript and their valuable comments and suggestions.

References

Bessell, M. S. [1990] *Pub. Astron. Soc. Pac.* **102**, 1181.
Ellerbroek, B. L., Adkins, S., Andersen, D. *et al.* [2012] *Proc. SPIE* **8447**, 84471J.
Ellerbroek, B. L. [2013] *J. Astrophys. Astr.* **34**, 121.
Fan, Z. Y., Plane, J. M. C., Gumbel, J. *et al.* [2007] *Atmos. Chem. Phys.* **7**, 4107.
Fugate, R. Q., Fried, D. L., Tyler, G. A. & Wopat, L. M. [1991] *Nature* **353**, 144.
Fuss, I. G. [1994] *IEEE J. Quantum Electron.* **30**, 2707.
Gumbel, J., Fan, Z. Y., Waldemarsson T. *et al.* [2007] *Geophys. Res. Lett.* **34**, L04813.
Happer, W., MacDonald, G. J., Max, C. E. & Dyson, F. J. [1994] *J. Opt. Soc. Am. A* **11**, 263.
Hedin, J. & Gumbel, J. [2011] *J. Atmos. Sol. Ter. Phys.* **73**, 2221.
Hickson, P., Pfrommer, T., Cabanac, R. *et al.*, [2007] *Publ. Astron. Soc. Paci.* **119**, 444.
Holzlöhner, R., Rochester, S. M., Bonaccini Calia, D., Budker, D., Higbie, J. M. & Hackenberg, W. [2010] *A & A* **510**, A20.
Jeys, T. H. [1991] *Lincoln Lab. J.* **4**, 133.
Kibblewhite, E. [2009] *Proc. Advanced Maui Optical and Space Surveillance Technologies Conf.*, S. Ryan, ed. (Curran Associates, 2009), p. E33.
Mansell, J. D., Hennawi, J., Gustafson E. K., *et al.* [2001] *Appl. Opt.* **40**, 366.
Oke, J. B & Schild, R. E., [1970] *APJ* **161**, 1015.
Patat, F. [2004] *Messenger* **118**, 11.
Pfrommer, T. & Hickson, P. [2010] *J. Opt. Soc. Am. A* **27**, A97.
Pfrommer, T. & Hickson, P. [2014] *A&A* **565**, 102.
Pfrommer, T., Hickson, P. & She, C.-Y. A. [2009] *Geophys. Res. Lett.* **36**, L15831.
Pickles, A. J. [1998] *Publ. Astron. Soc. Pac.* **110**, 863.
Plane, J. M. C., Gardner, C. S., Yu, J. R. *et al.* [1999] *J. Geophys. Res.* **104**, 3773.
Prasanth, P. V., Sivakumar, V., Sridharan, S. *et al.* [2009] *Ann. Geophys.* **27**, 3811.
Rochester, S., Otarola, A., Boyer, C. *et al.* [2012] *J. Opt. Soc. Am. B* **29**, 2176.
Roy, R. & Labeyrie, A. [1985] *A&A* **152**, L29.
Schoonover, R. W., Davis, B. J., Bartels, R. A. *et al.* [2008] *J. Mod. Opt.* **55**, 1541.
She, C. Y., Chen, S., Hu, Z. *et al.* [2000] *Geophys. Res. Lett.* **27**, 3289.
States, R. J. & Gardner, C. S., [1999] *J. Geophys. Res.* **104**, 11783.
Telle, J., Drummond, J., Hillman, P. & Denman, C. [2008] *Proc. SPIE* **6878**, 68780G.
von der Linde, D. [1986] *Appl. Phys. B* **39**, 201.
Wang, P.-Y., Xie, S.-Y., Bo, Y. *et al.* [2014] *Chin. Phys. B.* **23**, 094208.

J. Astron. Instrum. 2016.05. Downloaded from www.worldscientific.com
by CHINESE ACADEMY OF SCIENCES @ BEIJING on 12/13/17. For personal use only.